Ocean Modelling 000 (2015) 1–15

Contents lists available at ScienceDirect

Ocean Modelling

journal homepage: www.elsevier.com/locate/ocemod

Virtual Special Issue
Ocean Surface Waves

Projected wave conditions in the Eastern North Pacific under the influence of two CMIP5 climate scenarios

L.H. Erikson[a,*], C.A. Hegermiller[a,b], P.L. Barnard[a], P. Ruggiero[c], M. van Ormondt[d]

[a] United States Geological Survey, Pacific Coastal and Marine Science Center, 400 Natural Bridges Drive, Santa Cruz, CA 95060, USA
[b] University of California at Santa Cruz, Department of Ocean Sciences, 1156 High Street, Santa Cruz, CA 95064, USA
[c] Oregon State University, College of Earth, Ocean, and Atmospheric Science, 104 CEOAS Administration Building, Corvallis, OR 97331, USA
[d] Deltares-Delft Hydraulics, P.O. Box 177, 2600 MH Delft, The Netherlands

ARTICLE INFO

Article history:
Received 17 February 2015
Revised 28 June 2015
Accepted 7 July 2015
Available online xxx

Keywords:
Wave climate
GCMs
Climate change
Eastern North Pacific

ABSTRACT

Hindcast and 21st century winds, simulated by General Circulation Models (GCMs), were used to drive global- and regional-scale spectral wind-wave generation models in the Pacific Ocean Basin to assess future wave conditions along the margins of the North American west coast and Hawaiian Islands. Three-hourly winds simulated by four separate GCMs were used to generate an ensemble of wave conditions for a recent historical time-period (1976–2005) and projections for the mid and latter parts of the 21st century under two radiative forcing scenarios (RCP 4.5 and RCP 8.5), as defined by the fifth phase of the Coupled Model Inter-comparison Project (CMIP5) experiments. Comparisons of results from historical simulations with wave buoy and ERA-Interim wave reanalysis data indicate acceptable model performance of wave heights, periods, and directions, giving credence to generating projections. Mean and extreme wave heights are projected to decrease along much of the North American west coast. Extreme wave heights are projected to decrease south of ~50°N and increase to the north, whereas extreme wave periods are projected to mostly increase. Incident wave directions associated with extreme wave heights are projected to rotate clockwise at the eastern end of the Aleutian Islands and counterclockwise offshore of Southern California. Local spatial patterns of the changing wave climate are similar under the RCP 4.5 and RCP 8.5 scenarios, but stronger magnitudes of change are projected under RCP 8.5. Findings of this study are similar to previous work using CMIP3 GCMs that indicates decreasing mean and extreme wave conditions in the Eastern North Pacific, but differ from other studies with respect to magnitude and local patterns of change. This study contributes toward a larger ensemble of global and regional climate projections needed to better assess uncertainty of potential future wave climate change, and provides model boundary conditions for assessing the impacts of climate change on coastal systems.

Published by Elsevier Ltd.

1. Introduction

Coastal planners, managers, and engineers increasingly require information about climate change to make better planning decisions and minimize future coastal hazards and economic loss, potentially affecting millions of people residing near the coast (National Oceanic and Atmospheric Adminstration, 2010). General circulation models (GCMs) are now routinely used for assessing climatological parameters, including changes in storm patterns, atmospheric variability, temperatures, and precipitation (Barnes and Polvani, 2013; Cayan et al., 2008; Chang et al., 2013; Feng et al., 2014; Maurer et al., 2010; Sillmann et al., 2013), but these models generally do not provide parameterizations of ocean wind-waves (Cavaleri et al., 2012). To generate wave projections, a growing number of studies have used GCM-simulated near-surface wind or sea-level pressure fields for downscaling, in conjunction with either numerical or statistical methods (Hemer et al., 2013a; Mori et al., 2010; Semedo et al., 2013; Wang et al., 2014). Most of these downscaling efforts were conducted on global scales and focused on mean wave conditions. However, for the purpose of assessing coastal risk, there is a strong need to increase efforts toward understanding how climate change will influence extreme wave conditions on regional and local scales along coastlines (Barnard et al. 2014; Hemer et al., 2013a).

* Corresponding author. +18313259654.
E-mail address: lerikson@usgs.gov (L.H. Erikson).

http://dx.doi.org/10.1016/j.ocemod.2015.07.004
1463-5003/Published by Elsevier Ltd.

The wave climatology of the eastern North Pacific (ENP) is influenced by large-scale atmospheric patterns. During boreal spring and summer, wave conditions are driven by prevailing northwesterly winds and southern hemisphere storms (Allan and Komar, 2006; Bromirski et al., 2005; Graham and Diaz, 2001; Hemer et al., 2013b; Raible et al., 2005). For the rest of the year, ENP wave climatology is dominated by mid-latitude North Pacific cyclones, Eastern Pacific tropical storms, and local winds (Adams et al., 2008; Alves, 2006; Bromirski et al., 2005; Fan et al., 2013, 2012; Shimura et al., 2013). Swell and intermediate period waves with peak spectral wave periods (T_p) > 6 s dominate the wave energy spectrum throughout the year, especially during boreal winter when swell can be more than five times greater than local sea energy (Bromirski et al., 2005). Extreme events are linked to the Aleutian Low and other North Pacific atmospheric patterns (Graham and Diaz, 2001; Gulev and Grigorieva, 2006; Trenberth and Hurrell, 1994; Wang and Swail, 2001), such as the El Niño-Southern Oscillation (ENSO; Allan and Komar, 2006; Jien et al., 2015) and Arctic Oscillation (Thompson and Wallace, 1998). The Aleutian Low is a climatic feature of low atmospheric pressure centered near the Aleutian Islands (Mesquita et al., 2010) and represents one of the main centers of action in atmospheric circulation of the Northern Hemisphere.

Although Southern Ocean swell provides energy to the ENP wave climate (Alves 2006; Semedo et al., 2011), extreme wave conditions are typically dominated by swell generated by cyclones in the North Pacific during boreal winter (Bromirski et al., 2005; Bromirski et al., 2013; Cayan et al., 2009). Using reanalysis and *in situ* data, Graham and Diaz (2001) noted an increase in the frequency and intensity of December to March cyclones over the North Pacific Ocean, primarily west of the dateline between 30° and 40°N, during the latter half of the 20th century. Coincident with this time-period and extending into the first decade of the 21st century, a number of observation and reanalysis studies have also shown corresponding increases in significant wave heights (average value of top 1/3 wave heights, H_s) and wave period, particularly in the northern ENP (Allan and Komar, 2000; Bromirski et al., 2005; Gulev and Grigorieva, 2006; Menéndez et al., 2008; Ruggiero et al., 2010; Semedo et al., 2011; Wang and Swail, 2001). Yet some observation-based studies indicate weak decreasing signals or near-neutral wave conditions (Cayan et al., 2009; Gemmrich et al., 2011; Wang and Swail, 2001; Young et al., 2011). For the recent past, Sasaki (2014) also noted decreasing trends in both H_s and mean wave period (T_m) from 1992 to 2012 for most of the mid-latitude North Pacific (30–50°N, 150°E–110°W). North of 55°N, Sasaki (2014) identified increasing H_s and unchanging T_m along the Canadian and Alaskan coasts.

Projected 21st-century North Pacific cyclone activity has been examined with various GCMs and forcing scenarios (Favre and Gershunov, 2009; Ulbrich et al., 2009; Yin, 2005). Graham et al. (2013) provides a synthesis of such studies and suggests that cyclone activity is projected to decrease south of ~35 to 40°N, especially in the western Pacific Ocean where meridional gradients in cyclone activity are strongest. North of ~40°N, the studies indicate considerable spatial variability with respect to the east–west direction (Graham et al., 2013). Consistent with projected decreases in North Pacific cyclone activity, some studies have projected decreases in future ENP wave conditions. For example, using an ensemble (Fan et al., 2013; Hemer et al., 2013b; Mori et al., 2010; Semedo et al., 2013; Wang and Swail, 2006) of CMIP3 model projections, Hemer et al. (2013a) assessed changes in wave height, period, and direction by comparing end-of-21st century projections with a recent historical time-period (~1979 to 2009). Mean H_s and T_m were projected to decrease and increase, respectively, along ENP coasts, and incident mean wave directions (D_m) were projected to rotate counter-clockwise in the ENP. One study with a particular focus on the ENP (Graham et al., 2013) projected strong latitudinal dependencies along the mainland coast, with upper quantile H_s increasing north of ~40 to 50°N and decreasing to the south. In contrast, other studies have projected increasing trends in both mean and extreme H_s along nearly all ENP coasts, including south of ~40°N (Mori et al., 2013; Wang et al., 2014; Wang and Swail, 2006). The underlying causes for the contradictory results are not clear and may be related to factors including use of different methods of downscaling (dynamical or statistical), GCM forcing, and/or time-periods of comparison. Prior wave projection studies exhibit considerable variability within the ENP. Additionally, ENP coasts are heavily populated and have many coastal management and adaptation needs. Thus, specific attention to the ENP is required.

In this study, we use global and regional numerical wave models to quantify and assess projected trends in mean and extreme wave conditions within the ENP in response to the most recent Intergovernmental Panel on Climate Change (IPCC) climate scenarios. Recent historical (1976–2005) and future ENP wave conditions were dynamically-downscaled by forcing the WaveWatch III (WW3) numerical wave model (Tolman et al., 2002) on global (1.25° × 1°) and regional (0.25° × 0.25°) grids with GCM-simulated, near-surface (10 m height), 3-hourly wind fields under two representative concentration pathways (RCP) (RCP 4.5 and RCP 8.5) (Meehl and Hibbard, 2007; Moss et al., 2010; van Vuuren et al., 2011). Projected wave conditions for mid- and end-of-century time-periods (2026–2045; 2081–2100) were modeled; mean and extreme wave conditions are presented here from the combined 40-year 21st-century time-series. Because of high variability and uncertainty in GCM-simulated wind fields (Elguindi and Grundstein, 2013), four separate GCMs were used to force WW3 to develop future wave climate time series, and a multi-model mean was used to assess changes in projected wave conditions in response to radiative forcing scenarios.

This paper is outlined as follows. Details of the wave model and GCM-simulated winds are provided in Section 2: Data and Methods. Section 2 also includes explanations of the extreme value analyses employed and describes the method used for determining conditional relationships between wave parameters. In Section 3, model outputs from the historical time period are compared to ERA-Interim wave reanalysis values and wave buoy measurements within the ENP. Results pertaining to changes in near-surface winds and mean and extreme wave conditions are presented in Section 4. Finally, a summary and discussion of results and how they compare to previous studies are provided in Section 5, followed by conclusions in Section 6.

2. Data and methods

2.1. GCM-simulated near-surface wind data

Datasets of near-surface (10 m height) winds generated by four separate GCMs provided forcing to the wave model (Table 1). All global simulations used in this study follow the CMIP5 protocol for long-term simulations (Taylor et al., 2012). Only outputs from the first GCM simulation (r1) were used when multiple runs with differing initial conditions were available. Criteria for selection of the four GCMs were based on availability of projected near-surface winds

Table 1
CMIP5 GCM-simulated near-surface winds employed in this study.

Modeling center	Model	Model resolution
Beijing Climate Center, Meteorological Administration, China	BCC-CSM1.1	2.8° × 2.8°
Institute for Numerical Mathematics, Russia	INM-CM4	2.0° × 1.5°
Model for Interdisciplinary Research on Climate, Japan	MIROC5	1.4° × 1.4°
NOAA Geophysical Fluid Dynamics Laboratory, USA	GFDL-ESM2M	2.5° × 1.5°

to the year 2100, output frequency (3-hourly non-averaged synoptic winds), and completed GCM simulations at the onset of this study.

Wind data from three time-periods were used: 1976–2005 represents the post-industrial historical time-period, 2026–2045 represents the mid-21st century, and 2081–2100 represents the end of the 21st century. The mid- and end-of-century time-periods were simulated under RCP 4.5 and RCP 8.5. The scenarios represent trajectories of increasing global radiative forcing that reach, by the year 2100, +4.5 W/m^2 and +8.5 W/m^2 compared to pre-industrial (1850) conditions (Hibbard et al., 2007). RCP 4.5 and RCP 8.5 characterize medium stabilizing and high radiative forcing scenarios, respectively (Moss et al., 2010), and are roughly equivalent to the B1 and A2 emission scenarios of the IPCC CMIP3 Special Report on Emission Scenarios (SRES) (Meinshausen et al., 2011).

Grid resolutions of the GCM-simulated wind fields vary and, thus, were linearly interpolated to the wave model resolution. All winds were available as 10 m neutrally-stable fields and similar to many previous studies (Cheng et al., 2015; Dobrynin et al., 2012), no bias adjustments were made. It is noted here that Graham et al. (2013) found marked improvement when applying wind bias adjustments to CMIP3 wind fields. On the other hand, Hemer et al. (2013b) found no improvement in wave model results after bias adjustments of wind fields, though the wind fields used in that study were already dynamically-downscaled finer than the native GCM resolution.

2.2. Wave model

The third-generation, spectral wave model WaveWatch III (WW3; version 3.14; Tolman et al., 2002) was forced by historical and projected GCM-simulated winds. The model was applied over a near-global grid (NWW3; latitude 80°S–80°N) with 1° × 1.25° spatial resolution, and a nested ENP grid with 0.25° × 0.25° spatial resolution (~27 km at latitude 37°N; Fig. 1). Bathymetry and shoreline positions were populated with the 2-min Naval Research Laboratory Digital Bathymetry Data Base (DBDB2) v3.0 and National Geophysical Data Center Global Self-Consistent Hierarchical High-Resolution Shoreline (GSHHS; V1.7). Wave spectra were computed with 15° directional resolution and 25 frequency bands ranging non-linearly from 0.04 to 0.5 Hz. Wind-wave growth and whitecapping were modeled with the Tolman and Chalikov (1996) source term package and nonlinear quadruplet wave interactions were computed with the Hasselmann et al. (1985) formulation. In consideration of large data storage requirements, only daily averages of spatially-gridded H_s, peak period (T_p) and peak wave direction (D_p) were saved from the NWW3 and ENP grids. For extreme analysis, wave parameters (H_s, T_p, and mean wave direction, D_m) were saved hourly at 33 points along ENP coasts. The motivation for saving and assessing changes in H_s, T_p, and D_m was driven by the notion that storm impacts on coastal processes, including wave runup and erosion, are often investigated with these parameters (e.g., Bromirski et al., 2013). H_s and T_p are measures often used for calculation of runup (Ahrens, 1981; Mase, 1989; Stockdon et al., 2006; Van Der Meer and Stam, 1992), while D_m is a useful metric for wave-driven longshore sediment transport studies (e.g., Splinter et al., 2012).

2.3. Extreme value analysis of H_s

Design codes stipulate that both offshore and nearshore structures should be designed to exceed specific levels of reliability, usually expressed in terms of return periods (RP). For this reason, both return values (RV) and upper quantile (95th and 99th) wave conditions were computed for evaluation of changes in extreme wave climate.

Return values were calculated by fitting the generalized Pareto distribution (GPD) to identified extreme values and assuming stationary signals. Stationarity was assumed based on analysis of annual mean extreme wave heights at each of the 33 output stations. Least-squares linear fits indicate that for RCP 4.5 and RCP 8.5 combined mid- and end-of-century time-periods, only 9% of the stations exhibit statistically significant (p-Value < 0.05) trends. The time-series data of each climate scenario are thus predominantly stationary and as a result we assumed stationarity for extreme value analyses at all sites.

The GPD is commonly used for extreme value analysis of significant wave heights (Caires et al., 2006; Callaghan et al., 2008; Martucci et al., 2010; Méndez et al., 2006; Menéndez et al., 2008; Ruggiero et al., 2010). The cumulative distribution function of the GPD is given by

$$F_u(x) = \begin{cases} [1 + \kappa\sigma^{-1}(x-u)]^{1/\kappa}, & \kappa \neq 0 \\ exp(-(x-u)/\sigma), & \kappa = 0 \end{cases} \quad (1)$$

where u is the threshold and σ and k are the scale and shape parameters, respectively, obtained by maximum likelihood estimates. When $k = 0$, the GPD is the exponential distribution; when $k < 0$, it is the Pareto distribution; and when $k > 0$, it is a special case of the beta distribution (Caires and Sterl 2004). In this study, the GPD most

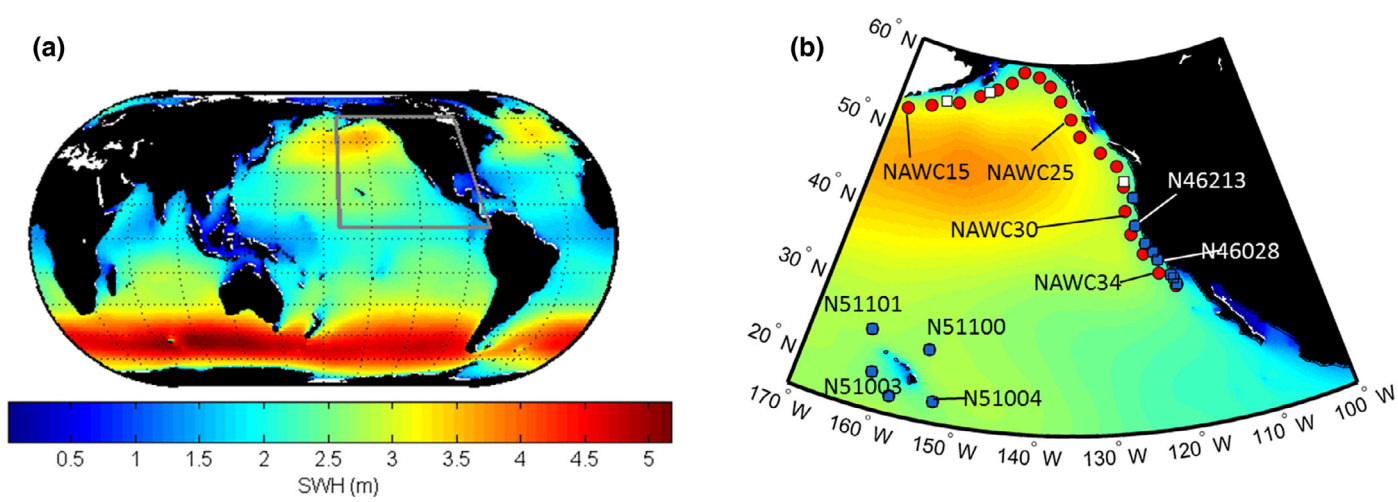

Fig. 1. Study area and wave model grid extents. Colormap depicts ensemble arithmetic mean of significant wave heights (H_s, m) for the 1976–2005 historical time-period. (a) Global grid extends from 85°S to 85°N with a 1°× 1.5° resolution. Gray outline represents the bounds of the one-way nested Eastern North Pacific (ENP) 0.25°×0.25° resolution grid. Daily averages of bulk parameters were saved from each of the grids. (b) Portion of ENP grid and coastal deep water stations (red filled circles) where model results were saved hourly. Squares indicate buoy measurement sites where model output locations were co-located (blue squares) and for which nearby output locations were used for comparisons (white squares). (For interpretation of the references to color in this figure legend, the reader is referred to the web version of this article.)

commonly took the form of the Pareto distribution, a finding similar to Izaguirre et al. (2011), who found similarly heavy-tailed behavior in swell-dominated areas not impacted by high cyclone or typhoon activity.

The GPD was fit through sets of 200 individual extreme wave events identified from the 40-year projection (20 years each at the mid- and end-of-century) of each separate GCM-forced wave time-series on the basis of allowing for an *average* of five independent events per year (40 years × 5 events/year on average = 200 events) – i.e., peak-over-threshold (POT). Independent events were defined as events that were at least three days apart, the approximate time scale of northeast Pacific extratropical storms (e.g., Méndez et al., 2006). Five events per year were selected based on work by Ruggiero et al. (2010), which found that extracting wave events greater than the 99.5th percentile of 30+ years of U.S. Pacific Northwest buoy measurements resulted in approximately 5 events per year.

Using the methods described above, eight return value curves were calculated for each location, one for each of the four GCM-forced wave time-series and each of the two radiative forcing scenarios, RCP 4.5 and RCP 8.5. For each scenario, return value curves from the four individual GCM-forced wave time-series were averaged at each location to obtain a multi-model return value curve relating H_s values to selected return periods (Fig. 2a). The four GCM-forced wave time-series were regarded as independent experiments and, as such, uncertainty associated with the multi-model curve was estimated as the standard deviation of the mean (σ_m),

$$\sigma_m = \frac{s}{\sqrt{N}}, \text{ where } s = \sqrt{\frac{\sum_{i=1}^{N}(x_i - \bar{x})}{N-1}} \tag{2}$$

where N is the number of sample points (4 in this case) and $x_i - \bar{x}$ is the deviation of each sample value from the arithmetic mean.

2.4. Extreme value analysis of T_p and D_m

There are two standard approaches to evaluating T_p and D_m: either as values independently derived from time series (i.e. the 99th percentile T_p (T_p^{99})) or as parameters that are conditionally related to H_s. In coastal design applications, a conditional relationship is typically used (e.g. Cheng et al., 2015) to avoid the occurrence of physically unrealistic conditions. In this study, we evaluate changes of extreme T_p and D_m in both ways: as independent and conditionally-varying parameters.

With the goal of finding a most likely (and physically realistic) T_p associated with a median or extreme wave height value, conditionally-related T_p were determined following a modification of an approach from Callaghan et al. (2008). Callaghan et al. (2008) modeled wave period variability using three parameter log-normal distributions described by H_s. Here, residuals decreased (better fits were found) when wave period variability is modeled with a normal distribution in which the mean, μ, and standard deviation, σ, are a function of H_s,

$$(\mu, \sigma) = \left(aH_s^b, \left(\frac{2c}{H_s}\right)^{.5}\right) \tag{3}$$

where a, b, and c are fitted parameters. Fig. 2b compares the mean T_p associated with 0.5 m H_s bins (yellow asterisks) with the expected value of T_p using the best fit parameters from Eq. (3) (blue line). The model reproduces both T_p limits and a reduction in variance as a function of increasing H_s (Fig. 2b). This approach allows for selection of an expected value of T_p associated with any extreme return value of H_s, as well as the 95% confidence intervals.

With the aim of identifying incident wave directions associated with extreme H_s, wave directions were derived from the joint

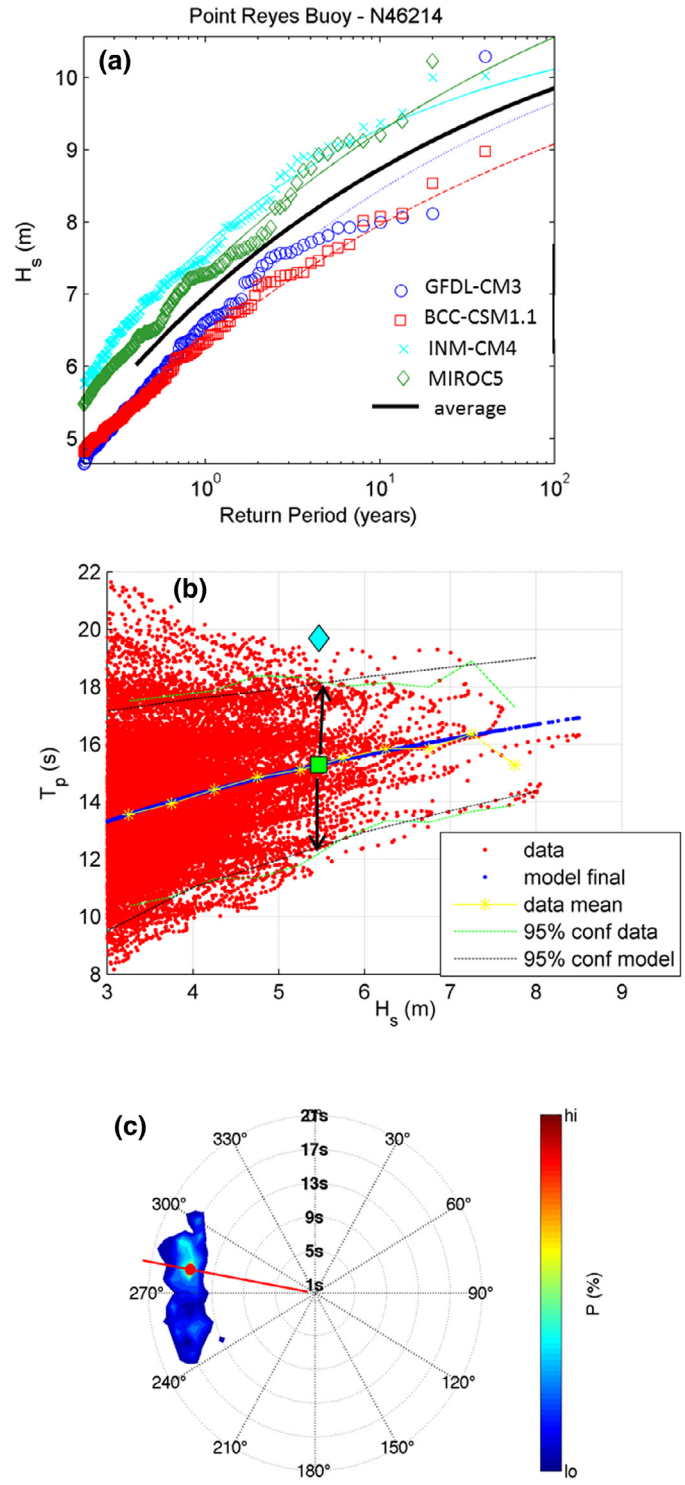

Fig. 2. Derivation of return period values of H_s, and dependent variables T_p, and D_m. Example plots are for RCP 4.5 at the Pt. Reyes buoy, N46214. (a) Return value plot using extreme H_s from each of the four GCM-forced wave simulations and the multi-model mean (black solid). (b) GFDL-ESM2M modeled T_p and H_s and Monte Carlo fitted normal line relating T_p to H_s. Blue diamond represents the 99th percentile H_s and T_p, note that it falls outside the cloud of occurrences. The conditionally dependent T_p, associated with the same 99th percentile H_s, is shown with the green square and 95% confidence interval (arrows). (c) Selection of D_m based on maximum probability of D_m for a given H_s return value (example is for the 5 year return period and all four GCM-forced wave simulations combined). (For interpretation of the references to color in this figure legend, the reader is referred to the web version of this article.)

probability of H_s and D_m. Probability density plots were generated for several coastal output stations from modeled time-series data binned at ±0.5 m, and 5° for H_s and D_m, respectively (Fig. 2c). Data from all four GCM-forced wave time-series were combined in each probability plot and D_m was obtained by finding the direction associated with the maximum probability of occurrence for the H_s of interest.

3. Model Evaluations

3.1. Spatial comparisons

The ability of the models to represent recent past mean wave climate was assessed by comparing results of the GCM-forced wave model with ERA Interim (ERAI), the latest global atmospheric reanalysis produced by the European Centre for Medium Range Weather Forecasts (Dee et al., 2011). ERAI wave parameters were produced from a coupled atmosphere–ocean wave model and high-resolution reanalysis winds. Post 1990 data includes wave spectra adjustments derived from satellite radar altimeter wave height data, and no adjustments with regard to buoy data. Mean H_s were calculated from ERAI archives of combined seas and swell at 6-hourly, 0.75° resolution. The time-period 1979–2005 was used in the comparison, as these are the years for which the ERAI data overlap with the GCM-forced historical wave simulations conducted as part of this study. For comparison with the GCM-forced historical wave simulations, ERAI was interpolated onto the WW3 ENP grid.

Compared to ERAI, three of the four GCM-forced wave simulations overestimate ENP annual mean H_s ($\overline{H_s}$; Fig. 3). The largest negative bias is obtained with GFDL-ESM2M, which underestimates by an average of −0.06 ± 0.06 m for the entire domain; the largest positive bias, accounting for both the spatial average and standard deviation, is obtained with MIROC5, for which the bias is 0.5 ± 0.22 m. The maximum biases attained at any grid point for these two models are 0.66 m and 0.88 m, respectively. Coastal regions are somewhat underestimated with GFDL-ESM2M and BCC-CSM1.1 and overestimated with MIROC5 and INM-CM4. The multi-model mean yields a lower combined bias and standard deviation compared to any of the individual models (0.05 ± 0.04 m), with a maximum <0.25 m along the mainland coast (Fig. 3e). All the models, and hence the multi-model mean as well, over-estimate $\overline{H_s}$ in the region surrounding Hawaii.

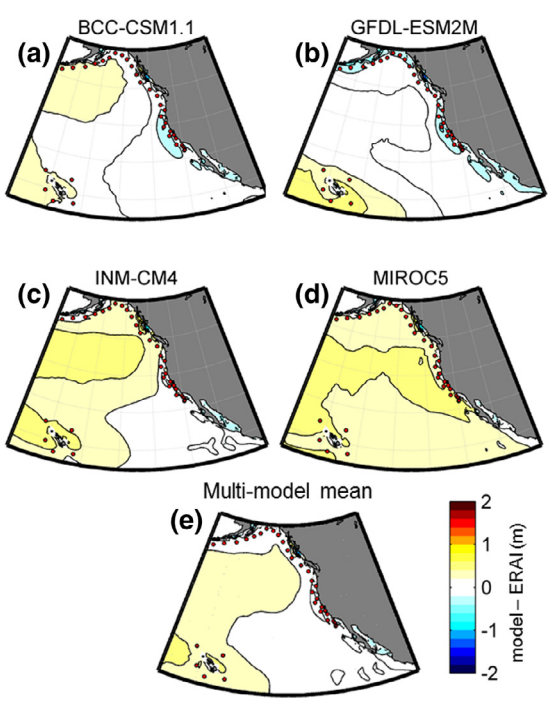

Fig. 3. Model bias with respect to ERAI reanalysis (model – reference) of mean H_s for all months spanning years 1979 through 2005: (a) BCC-CSM1.1, (b) INM-CM4, (c) GFDL-ESM2M, (d) MIROC5, and (e) multi-model mean. Positive values indicate that the GCM model over-estimates ERAI.

3.2. Point comparisons

Hourly wave conditions are compared to observation data from 15 buoys (Table 2) and ERAI data extracted from the closest grid cell to each of 33 coastal stations. Only buoys located in water depths greater than ~300 m (Graham et al., 2013) and distant from the coast are used for comparison with modeled waves to avoid land-sea interactions (e.g., orographic, katabatic) that could affect the wind fields (Chawla et al., 2013). In shallower water depths and/or closer to land, bathymetric and topographic interactions become important. These interactions are poorly simulated given the coarse resolution of the model.

Buoy data through the year 2005 are used. Depending on the particular buoy, the record lengths range from ~1 year (2004–2005 at NDBC46089) to 22 years (1983–2005 at NDBC46028) (Table 2). The observation records suffer from significant data gaps. Thus, co-located model output data were interpolated to the observation time stamps. To avoid unequally weighting the model data, we followed the analysis of Allan and Komar (2006), in which we omit all model and observation data in years when less than 80% of the winter (November–March) observation data were available.

For comparison of extremes, we limit the analysis to the months of November through March, when ENP extreme wave events typically occur (Bromirski et al., 2005). The timing of wave events modeled with GCM-simulated winds will not coincide precisely with observations. The discrepancy in timing is largely due to internal variations within the GCM runs and the fact that historical GCM runs are initiated from arbitrary times of quasi-equilibrium control runs (Taylor et al., 2012). In order to reduce the impact of precise timing between events, differences between model and reference (either observation or ERAI reanalysis), data are quantified by calculating the bias (model minus reference), root-mean-square difference (*RMSD*), and normalized variance (γ^2) from the cumulative distributions. *RMSD* is given by

$$RMSD = \sqrt{\frac{\sum_1^N (obs_i - mod_i)^2}{N}} \tag{4}$$

where obs_i is the observed value and mod_i is the modeled value of the ith occurrence, and N is the total number of bins (probabilities are graduated from 0.00 to 1.00 with a bin size of 0.01 resulting in $N = 101$). Normalized variance indicates the relative amplitude of modeled and observed variability and is given by

$$\gamma^2 = \gamma^2_{mod}/\gamma^2_{obs} \tag{5}$$

where γ^2_{mod} and γ^2_{obs} are the modeled and observed variances, respectively.

Biases between observed and modeled cumulative distributions were computed at each buoy station and bin-averaged across all sites, providing a coast-wide representation of bias as a function of probability of occurrence (Fig. 4). Three of the four GCM-forced wave simulations underestimate H_s at the lower tails of the distributions and overestimate H_s at the upper tails. GFDL-ESM2M consistently underestimates H_s, though bias approaches zero at the upper quantiles (Fig. 4a). The multi-model mean H_s bias at the 99th percentile is +0.5 m, and viewed in this manner does not perform as well as GFDL-ESM2M. All four models underestimate T_p in the upper quantiles and overestimate T_p in the lower quantiles (Fig. 4b). The multi-model

Table 2
Observational wave buoys used for comparison to modeled wave parameters (listed from north to south). Shading highlights buoy locations in the Pacific Northwest and Alaska, California, and Hawaii.

NDBC ID	Buoy owner[a]	time-period used in analysis[b]	Lat (DD,N)	Lon (DD,W)	Depth (m)
46078	NDBC	2004–2005	56.074	152.572	3405
46205	ENVCA	1990–2005	54.170	134.330	2675
46075	NDBC	2004–2005	53.911	160.806	2487
46208	ENVCA	1990–2005	52.517	132.668	2950
46089	NDBC	2004–2005	45.893	125.819	2289
46213	SCRIPPS	1999–2005	40.294	124.740	325
46214	SCRIPPS	1996–2005	37.945	123.470	550
46042	NDBC	1987–2005	36.789	122.404	1574
46028	NDBC	1983–2005	35.741	121.884	1158
46069	NDBC	2003-2005	33.670	120.200	1021
46219	SCRIPPS	2000–2005	33.221	119.882	335
46047	NDBC	1991–2005	32.403	119.536	1399
51003	NDBC	1984–2005	19.348	160.621	4919
51004	NDBC	1984-2005	17.525	152.382	5082
51002	NDBC	1984-2005	17.094	157.808	5002

[a] NDBC: National Oceanic and Atmospheric Administration's National Data Buoy Center, Stennis Space Center, MS, USA SCRIPPS: Scripps Institute of Oceanography, La Jolla, CA, USA ENVCA: Environment Canada, Gatineau, QC, Canada.
[b] Extensive data gaps in the observation set were identified and removed from the model time-series prior to comparisons; H_s and T_p data were used even in cases when directional data was not available.

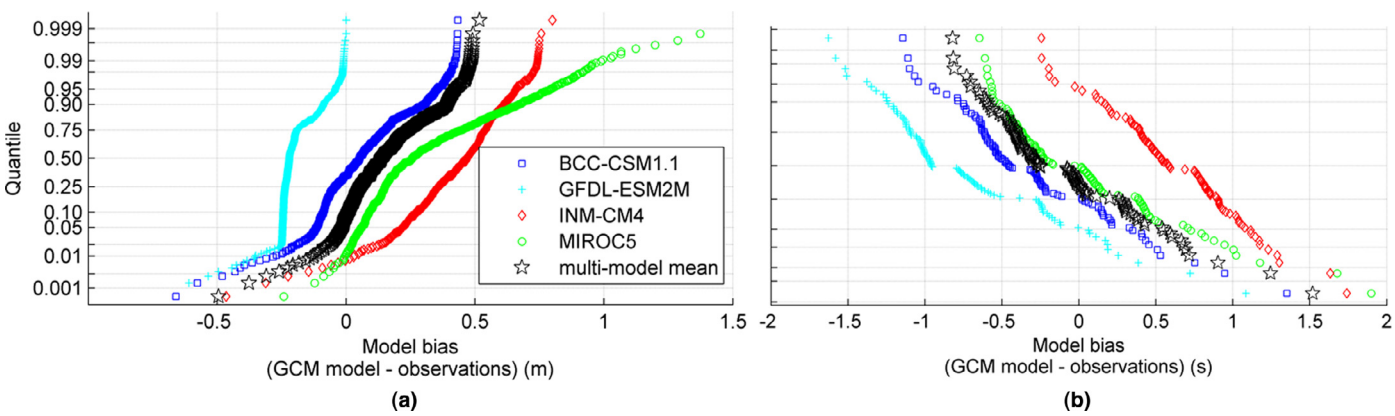

Fig. 4. Model bias with respect to wave buoy observations (model – reference) in the coastal region as a function of quantiles for winter months of November through March. Biases represent the average of 15 buoys for (a) H_s and (b) T_p. See Table 2 and Fig. 1 for buoy locations. Data are plotted on a log-normal probability scale for better visualization of the extremes.

mean T_p bias approximates zero near the median and is slightly less than −1 s at the 99th percentile.

A more spatially-detailed site-by-site depiction of H_s bias is presented in Fig. 5a and c. Here, the H_s bias (model – reference) at each coastal station was computed as the average difference between cumulative distributions of the model and reference data (Fig. 5). Data from the same 15 buoys presented above were used (Fig. 5a); ERAI data at the 33 coastal stations, inclusive of the 15 buoy locations, were also used (Fig. 5c). A striking difference between the biases is apparent. The multi-model mean exhibits very small bias with respect to buoy data at ∼35°N and underestimates H_s along the remainder of the coast. With respect to ERAI data, the multi-model mean overestimates H_s along the entire coast. The difference is related to the tendency of ERAI to underestimate larger wave heights (e.g., Stopa and Cheung, 2014), such as those represented here through limitation of the analysis to ENP winter wave conditions. Area-wide average biases are −0.15 m and +0.32 m for model-observation and model-ERAI comparisons, respectively. Associated *RMSD*s are 0.27 m and 0.51 m (Figs. 5b and d).

A similar evaluation of T_p shows a ±1 s scatter in the bias about zero when using observation data as the reference dataset (Fig. 6). GCM-forced wave simulations underestimate T_p by ∼1 s in comparison to ERAI. Normalized variances are at most 1.6 and average 1.3, indicating slightly greater variance in the simulated wave periods compared to observations (Table 3). Directional data is somewhat limited at the selected buoys with data available only at seven stations, located between ∼32 and 46°N. *RMSD* ranges between 4 ± 1.8° and 9 ± 2.2°. Normalized variances are again positive with a mean of 1.6, indicating greater variance in the simulated wave directions than in observations.

The largest discrepancies are at the northern end of the study site and surrounding the Hawaiian Islands. Generally higher errors in the north may be due to unprecisely located model output stations which were in some cases up to a couple hundred kilometers from actual buoy locations (stations marked with superscripts in Table 3). Bias surrounding the Hawaiian Islands might be related to the close proximity of these stations to ENP grid boundaries, which was one-way nested in the NWW3 grid (Fig. 1) or insufficient grid resolution for capturing wave shadowing or bathymetric change. Though 0.25° resolution does provide blocking of wave energy (note lower H_s south of Hawaii in Fig. 1 for example) and yields improved results compared to the global grid (not shown), further refinement would likely improve the results.

Though there are discrepancies between the multi-model mean and reference datasets, error statistics are within the range of other studies involving dynamical-downscaling using GCM-simulated

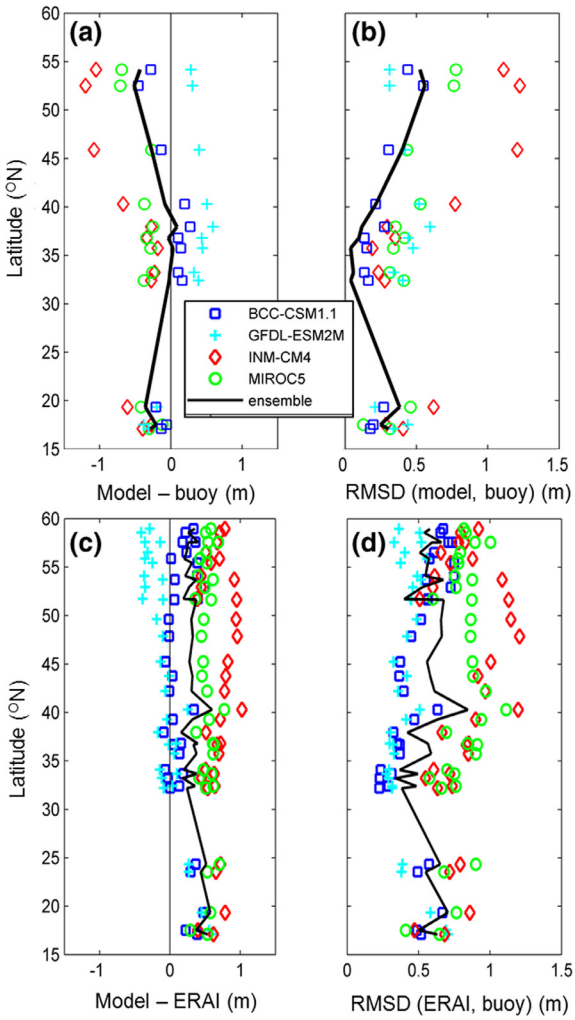

Fig. 5. Mean model bias and *RMSD* of winter (November through March) H_s as a function of latitude. (a, b) Bias and *RMSD* referenced to observational data from 15 buoys. See Table 2 and Fig. 1 for buoy locations. (c, d) Same as (a, b), but with ERAI as the reference data and including all 33 coastal stations.

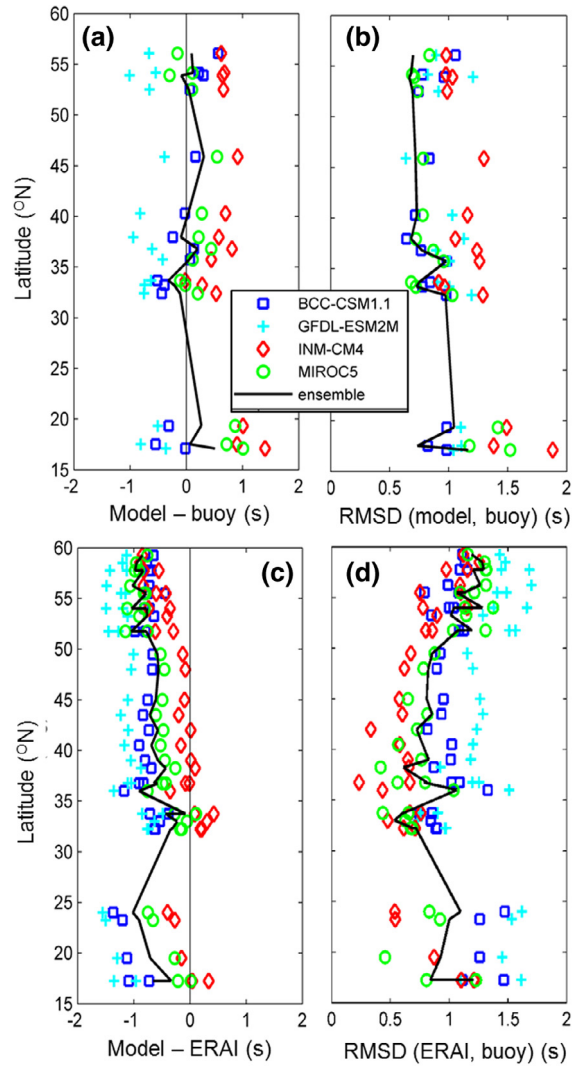

Fig. 6. The same as in Fig. 5 but for T_p.

Table 3
Error statistics of observed and modeled winter (November through March) wave conditions. Modeled conditions represent the multi-model mean.

NDBC ID	H_s		T_p		D_m	
	RMSD (cm)	γ^2 (dimensionless)	*RMSD* (s)	γ^2 (dimensionless)	*RMSD* (deg)	γ^2 (dimensionless)
46078[a]	26	0.8	0.7	1.2	ND	ND
46205[a]	50	0.7	0.7	1.0	ND	ND
46075[a]	13	1.0	0.7	1.1	ND	ND
46208[a]	53	0.7	0.7	0.9	ND	ND
46089[a]	52	0.6	0.7	1.4	7	2.5
46213	34	0.6	0.7	1.5	9	2.2
46214	15	0.7	0.7	1.5	9	1.4
46042	16	0.8	0.8	1.5	7	2.0
46028	18	0.8	1.0	1.8	4	1.8
46069	17	0.7	0.7	1.4	5	0.7
46219	9	0.8	0.7	1.4	7	0.5
46047	7	0.9	1.0	1.6	ND	ND
51003	43	0.6	1.0	1.4	ND	ND
51004	26	0.7	0.7	1.1	ND	ND
51002	33	0.7	1.2	1.3	ND	ND

[a] Model output point located between ~100 km to ~200 km from observation buoy. ND: no data.

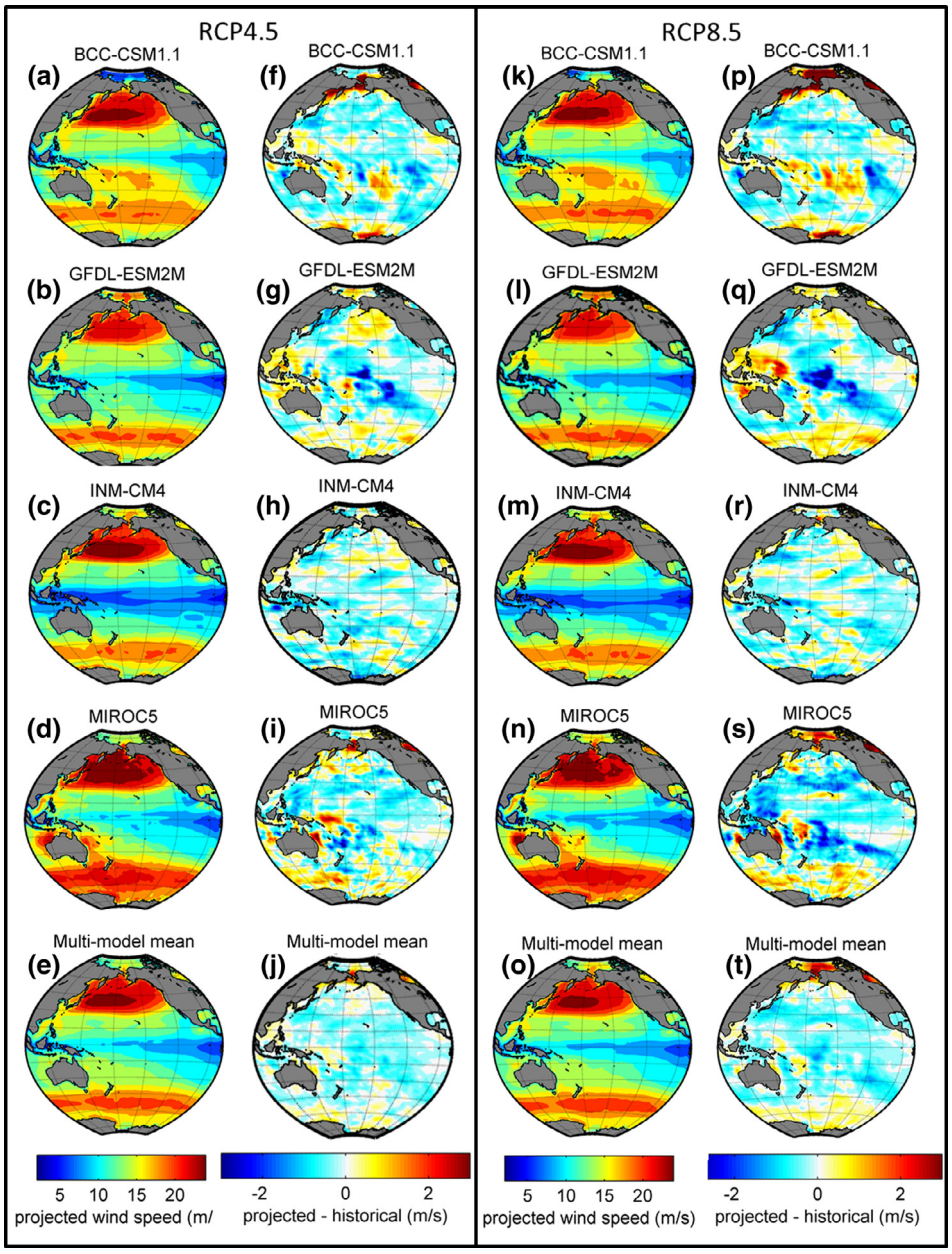

Fig. 7. GCM-simulated 99th percentile near-surface (10 m height), boreal winter (DJF) wind speeds under RCP 4.5 (left panel) and RCP 8.5 (right panel). (a–d) 99th percentile wind speeds for BCC-CSM1.1, GFDL-ESM2M, INM-CM4, and MIROC5 under RCP 4.5 for years 2026–2046 and 2081–2100. (e) Multi-model mean of a–d. (f–j) 99th percentile wind speeds in a–d (projected) minus 99th percentile wind speeds of respective, or multi-model mean, GCM for years 1976–2005. Right panel: the same as in left panel but under RCP 8.5.

winds (e.g., Hemer et al., 2013a). Comparisons of results from the GCM-forced wave simulations with buoy observations and ERAI reanalysis indicate that the model is capable of producing realistic patterns in space and time, providing confidence in the ability of the model to simulate a realistic climate change signal.

4. Results

4.1. Projected changes in near-surface winds

Because changes in projected wave climate ultimately stem from changes in projected surface winds, it is useful to examine GCM-simulated wind fields. Future extreme wind conditions, represented by the 99th percentile (U^{99}), were computed for each of the GCMs and compared to the respective historical extreme wind conditions (Fig. 7). Upper quantiles represent boreal winter wind speeds (December–February) from the combined mid- and end-of-century simulations.

All projected GCM-simulated wind fields follow general patterns consistent with present or historical storm conditions. Highest over-ocean winds are in the North Pacific, followed by lower, but still substantial speeds in the Southern Ocean (Fig. 7a–e and k–o). The highest wind speeds in the region of the Aleutian Low are located toward the western North Pacific in BCC-CSM1.1, GFDL-ESM2M, and INM-CM4. A broader area with higher wind speeds spans most of the North Pacific in MIROC5 (Fig. 7 a–d). Patterns are similar under both RCP 4.5 and RCP 8.5 (Fig. 7a–d and k–n), but magnitudes differ depending on location.

All four models largely project decreasing U^{99} in the mid-Pacific equatorial region, increases in the Southern Hemisphere, and regional patches of increasing and decreasing U^{99} in the North Pacific (Fig. 7f–i and p–s). A common region of projected U^{99}

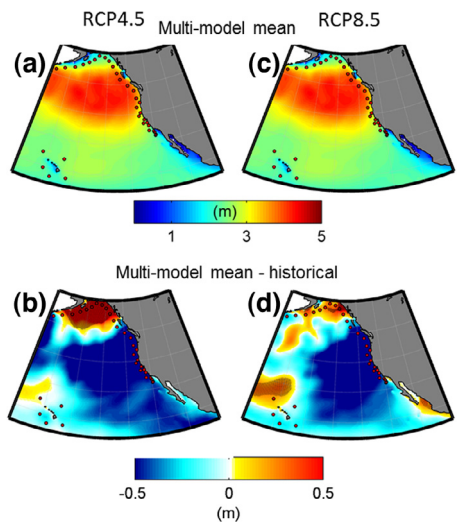

Fig. 8. Projected multi-model mean H_s under (a) RCP 4.5 and (c) RCP 8.5 and (b,d) the difference compared to the historical time-period (1976–2005). Multi-model means are from BCC-CSM1.1, GFDL-ESM2M, INM-CM4, and MIROC5. Projected conditions are for the multi-model mean over all months representing the mid- (2026–2045) and end-of-21st century (2081–2100) time-periods. The black '+' signs in (b, d) indicate areas where projected change is greater than the inter-model standard deviation. Red filled circles denote model output point locations where parameters were saved hourly. (For interpretation of the references to color in this figure legend, the reader is referred to the web version of this article.)

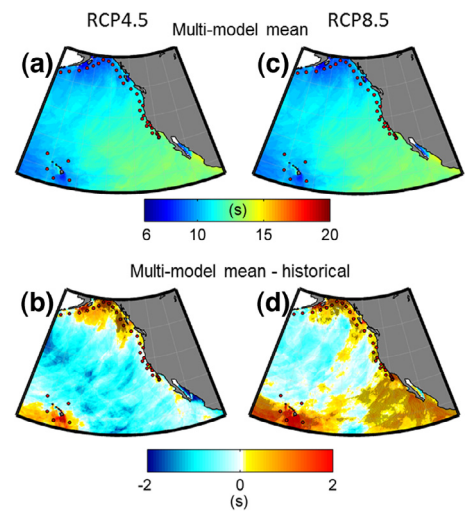

Fig. 9. The same as in previous but for T_p.

increase during boreal winter amongst all models, except INM-CM4, is north/northwest of Australia. Specific to the ENP coast, U^{99} is projected to decrease along most of the U.S. mainland coast and increase north along the Canadian and southern Alaskan coasts. Considering the multi-model means (Fig. 7j and 7t), the entire Pacific basin is projected to experience decreasing U^{99}, except in the Southern Ocean, northwest of Australia, and in the vicinity of the Aleutian Low, where increases are projected. The patterns are similar for both RCP 4.5 and RCP 8.5, but more pronounced with the latter scenario. While less relevant for ENP storm climatology, the projected increase in U^{99} over the Arctic Ocean (Beaufort and Chukchi Seas) is noteworthy.

4.2. Projected changes in mean wave statistics throughout the ENP

Projected multi-model $\overline{H_s}$ under RCP 4.5 and RCP 8.5 (Fig. 8a, and c) exhibits patterns that are similar to historical observations (Allan and Komar, 2000; Bromirski et al., 2005) and projected wave heights (Graham et al., 2013). Higher wave heights are projected in the northern ENP (~40 to 50°N) and lower wave heights to the south. A wave shadow zone is evident along the southern Alaskan coast. Projected changes are evaluated by subtracting modeled historical $\overline{H_s}$ from RCP 4.5 and RCP 8.5 $\overline{H_s}$ (Fig. 8b, and d). The pattern that emerges roughly reflects projected changes in near-surface winds (see previous section). $\overline{H_s}$ are projected to increase along the southern Alaskan coast and northwest of Hawaii, and to decrease elsewhere. An exception is along the Central American coast south of Baja, California, where $\overline{H_s}$ are projected to decrease and increase under RCP 4.5 and RCP 8.5, respectively. The stippled areas in Fig. 8 indicate where the magnitude of the multi-model mean exceeds the inter-model standard deviation. Inter-model standard deviation serves as a measure of agreement among the four projections. Agreement is high in regards to increasing $\overline{H_s}$ along the Aleutian Islands and southern Alaskan coast under RCP 4.5. Under RCP 8.5, there is also agreement, but over a much smaller region. Northeast of Hawaii, there is inter-model agreement of increasing $\overline{H_s}$ under RCP 8.5.

Projected multi-model annual mean T_p ($\overline{T_p}$) show similar patterns under RCP 4.5 and RCP 8.5 (Fig. 9a, and c) that are consistent with previous studies using observations (Allan and Komar, 2000) and models (Hemer et al., 2013a). For both sets of simulations, $\overline{T_p}$ are shorter in the northern ENP. Within the southwestern ENP, $\overline{T_p}$ are longer (Fig. 9a, and c) and likely reflect greater contributions of wave energy from Southern Ocean swell (Alves, 2006; Semedo et al., 2011). Compared to historical wave conditions, $\overline{T_p}$ are projected to increase near Hawaii and along much of the Alaskan and Canadian coasts under RCP 4.5. The higher radiative forcing scenario, RCP 8.5, is projected to have a greater influence with respect to both magnitude and space. Of note are the southwest facing coasts of Hawaii, California, and Central Mexico, where significant increases in $\overline{T_p}$ are projected (Fig. 9b, and d).

4.3. Projected changes in extreme wave conditions along the ENP coasts

For assessing projected changes of extreme wave conditions, we turn to the hourly data extracted from the model at 33 locations along the coasts. Upper 95th and 99th quantiles of historical multi-model means show that maximum wave conditions occur at ~52°N, offshore of British Columbia, Canada (Fig. 10a). North of ~52°N, 95th and 99th percentile H_s (H_s^{95} and H_s^{99}, respectively) decrease with increasing latitude, and south of ~52°N, extreme wave heights decrease with decreasing latitude along the mainland coast. H_s^{95} and H_s^{99} on the north and south sides of Hawaii are comparable to Central and Southern California, respectively. The two sites north of Hawaii are fully exposed to North Pacific storms, whereas the three sites on the south side are within the shadow zone of the Islands (Figs. 1b and 8a, and c) and thus under less influence of North Pacific storms.

Projected changes in upper quantile H_s are evaluated by subtracting historical multi-model extremes from future multi-model extremes under RCP 4.5 and RCP 8.5 (Fig. 10b, and c). H_s^{99} are projected to decrease south of ~50°N under RCP 8.5. With the exception of the Hawaii sites, decreases are projected under RCP 4.5 as well. The greatest change is at ~40°N, where H_s^{99} decreases of 0.45 m are projected under RCP 8.5. Larger decreases are projected under RCP 8.5 than under RCP 4.5, and inter-model agreement is greater under RCP 8.5 for H_s^{99} (Fig. 10b, and c). The sites surrounding the Hawaiian Islands are projected to experience increasing H_s^{99} under RCP 4.5, but little to no change under RCP 8.5. Extreme analysis represented with return values yields similar results, but with some notable differences (Fig. 10e–h, note the different x-axes scales). Projected changes in annual RVs are similar in both space and magnitude to projected changes in H_s^{99} (Fig. 10c, and e), but extrapolation to 50-year and 100-year RPs indicates greater decreases along the U.S. mainland coast from ~45°N southward under RCP 8.5.

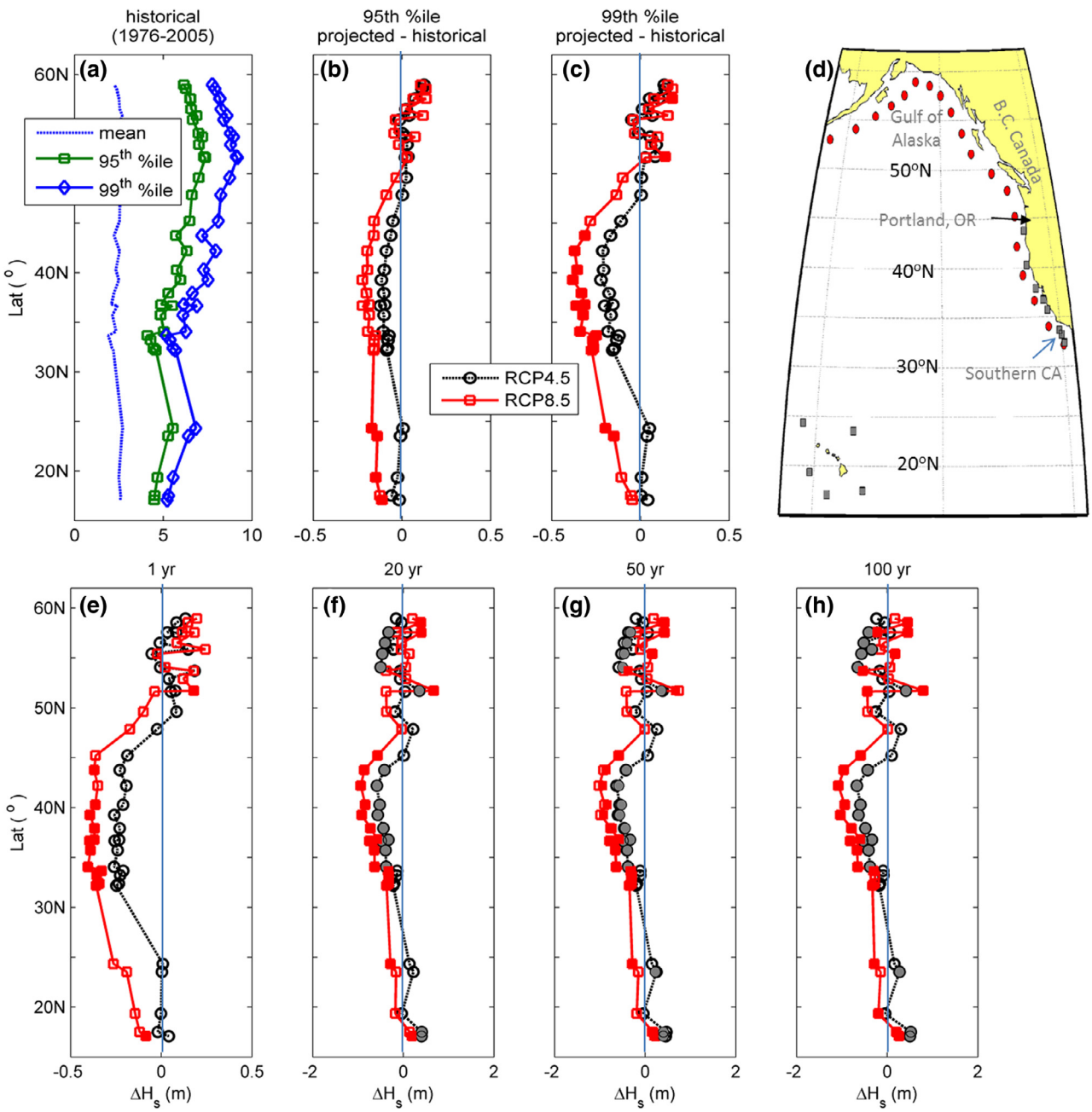

Fig. 10. Mean and extreme historical H_s and projected change in H_s along the ENP coasts under RCP 4.5 and RCP 8.5. (a) Historical mean and upper quantiles. (b,c) Projected change in upper quantile H_s. (d) Locations of points used in analysis. (e–h) The same as in (b, c), but for the annual, 20 year, 50 year, and 100 year return periods. Filled symbols in (b, c), and (e–f) indicate that the projected change is greater than the inter-model standard deviation. Note the different *x*-axes scales in (e–h).

Table 4
Percent change (projected – historical) in multi-model H_s north and south of ~53°N.

		Mean	Median	1 year	5 year	10 year	20 year	50 year	100 year	95th	99th
RCP4.5-historical	North	0.0	2.0	0.6	−0.9	−1.6	−2.4	−3.4	−4.2	0.5	0.2
	South	0.1	1.1	−2.0	−1.9	−1.7	−1.4	−1.0	−0.5	−1.1	−1.8
RCP8.5-historical	North	−0.5	1.6	1.3	1.2	1.1	0.9	0.7	0.6	0.8	0.7
	South	−1.5	−1.3	−4.1	−4.5	−4.6	−4.5	−4.4	−4.3	−2.6	−3.7

Though south of ~50°N, extreme H_s are projected to be smaller under RCP 8.5 than under RCP 4.5 compared to the historical, north of this latitude, differences between extreme H_s under RCP 4.5 and RCP 8.5 are much less and reversed. The reversal is accentuated in analysis of RVs, where changes in RVs under RCP 4.5 are more negative than changes in RVs under RCP 8.5 north of ~50°N, in contrast to the southern part of the study area (Fig. 10f–h). Averaged over the region south of ~50°N, extreme H_s are projected to decrease by 0.5–2% and 2.6–4.6% under RCP 4.5 and RCP 8.5, respectively (Table 4).

Because the latitudinal plots are difficult to decipher in the northern part of the study area where the coastline orientation rotates, it is helpful to view the projected changes spatially. With the exception

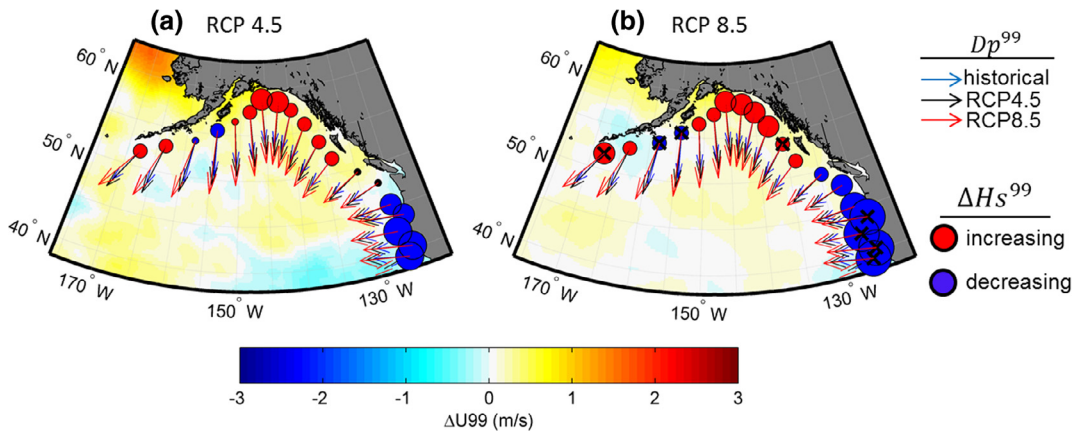

Fig. 11. Projected changes in 99th percentile H_s (projected – historical, ΔH_s^{99}) and associated incident wave directions, D_m^{99}, in the northern section of the study area under (a) RCP 4.5 and (b) RCP 8.5. Red and blue circles denote projected increases and decreases, respectively; size represents relative change. A black 'x' indicates inter-model agreement in whether H_s is increasing or decreasing. Arrows are scaled for viewing (not intensity) and point toward incident wave directions to enhance readability. Background colors represent the change in 99th percentile wind speeds for the months of November through March. (For interpretation of the references to color in this figure legend, the reader is referred to the web version of this article.)

of two stations, H_s^{99} under RCP 4.5 are projected to increase along the entire southern Alaskan coast and decrease further south, with a transition zone at ~50°N (Fig. 11a). The largest increases are projected for the south-facing embayment where greater increases in U^{99} are projected compared to the rest of the region. Projected increases in H_s^{99} are likely associated with increasing local U^{99} (warm background colors in Figs. 7j, and t and 11), as well as distant North Pacific storms providing increased swell energy.

Upper quantile incident wave directions (D_m^{99}) exhibit little change along most of the Gulf of Alaska coast except at the most easterly points along the Aleutian Islands, where they are projected to rotate as much as 10° clockwise under RCP 8.5 (Fig. 11b). Inter-model agreement is significant along the eastern stations giving confidence in northward and/or westward displacement of major storm tracks, which has been noted in previous work (Favre and Gershunov, 2009; Graham and Diaz, 2001; Graham et al., 2013; Yin, 2005).

Referring to projected changes in D_m throughout the remainder of the study area (Fig. 12), incident wave directions associated with H_s^{99} are projected to rotate clockwise at ~53°N by as much as 9° (note filled marker, Fig. 12b), change slightly at the mid-latitudes (30 –50°N), and rotate counter-clockwise offshore of Southern California. This latter result is somewhat counter-intuitive to what one might expect under conditions of more northerly-located storm centers (Graham et al., 2013; Mori et al., 2013). A possible explanation might be that storm energy from the historically dominant westerly and northwesterly storms will be reduced along the Southern California coast as these systems travel poleward. Simultaneously, energy contributions from Southern Ocean swell are projected to increase (Hemer et al., 2013a; Mori et al., 2010; Semedo et al., 2013; Wang and Swail, 2006), possibly resulting in a regime shift and counter-clockwise rotation of D_m^{99} in this region. This speculation might be better supported with the use of incident wave directions associated with peak energy, D_p, rather than *mean* directions; however, D_p were not available at the time of this analysis and thus more detailed analyses are left for future work. Upper quantile wave periods are projected to increase along the entire coast under both RCP 4.5 and RCP 8.5 (Fig. 13a–c). Historical T_p^{95} and T_p^{99} range from 17.6 ± 0.5 s to 19.3 ± 0.4 s and are 6–8 s longer than historical mean T_p

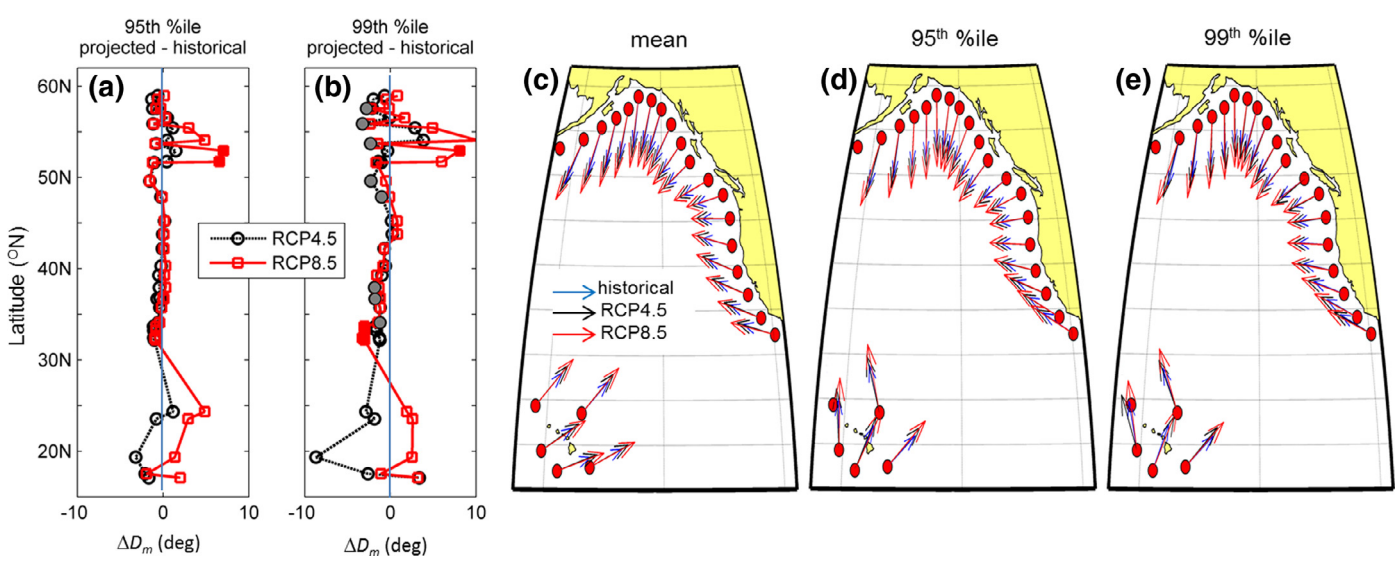

Fig. 12. Projected changes in incident wave directions along the ENP coast associated with multi-model mean and extreme H_s under RCP 4.5 and RCP 8.5. (a, b) Estimated change in direction (projected – historical) plotted as differences with respect to latitude. Filled symbols indicate that the change is greater than the inter-model standard deviation. (c–e) Incident wave angles associated with $\overline{H_s}$, H_s^{95}, and H_s^{99} for the historical time-period and projected RCP 4.5 and RCP 8.5 scenarios. Arrows are scaled for viewing (not magnitude) and point toward incident wave directions to enhance readability.

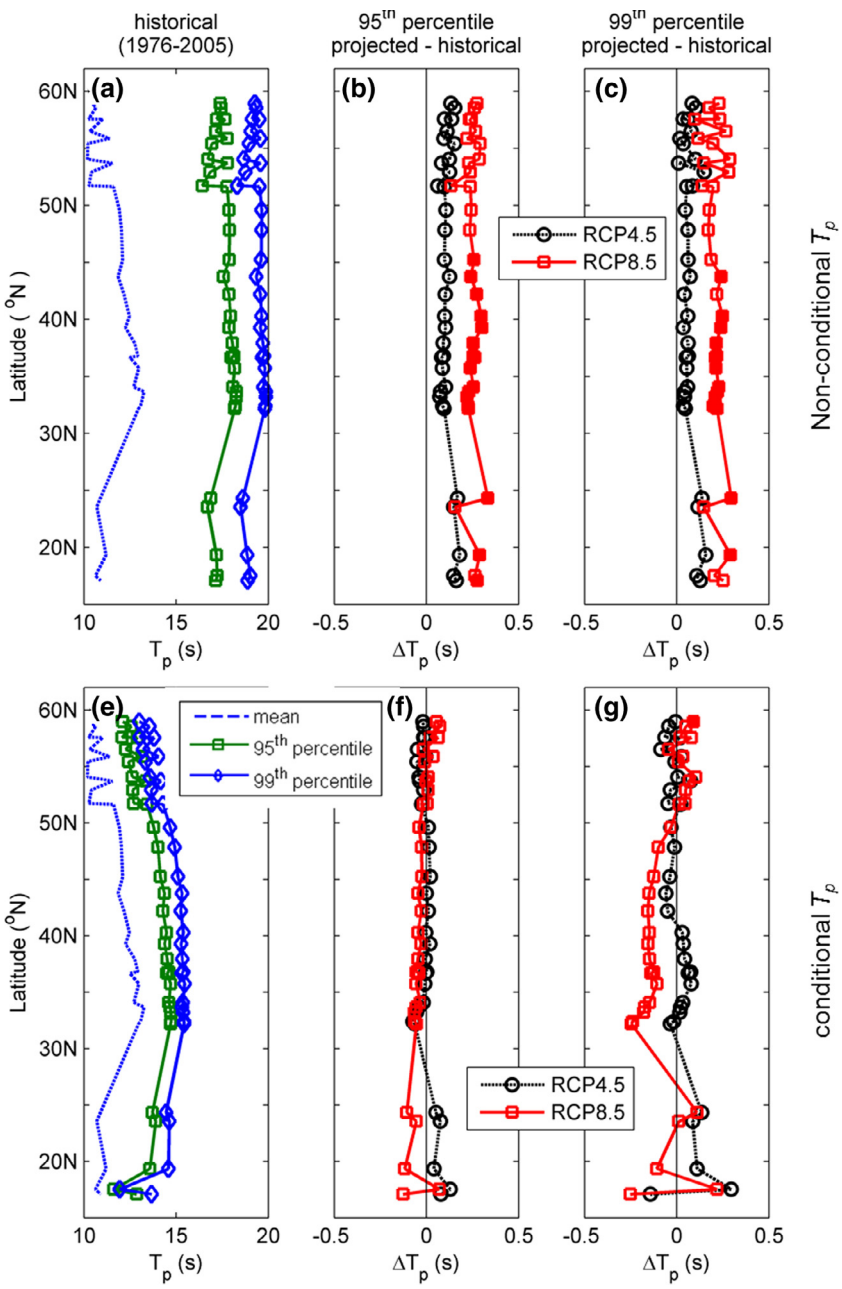

Fig. 13. Mean and extreme historical T_p and projected change along the ENP coasts under RCP 4.5 and RCP 8.5. (a) Historical mean and upper quantiles. (b, c) Projected change in the 95th and 99th percentile T_p. (d–f) The same as in a–c but for a 'most-likely' T_p, as derived from a conditional relationship with H_s.

(Fig. 13a). Projected changes are small, but are larger under RCP 8.5 (0.21 ± 0.05 s) than under RCP 4.5 (0.07 ± 0.04 s; Fig. 13b, and c). Inter-model agreement is also largest under RCP 8.5, particularly south of ~45°N (Fig. 13b, and c). Compared to annual mean $\overline{\Delta T_p}$ (Fig. 9b, and d), projected changes in upper quantile wave periods are very small (<0.5 s versus 2+ s).

Treating T_p as a conditional parameter associated with upper quantile H_s yields similarly small magnitudes of change (−0.13 ± 0.19 s; Fig. 13d–f). Conditionally-derived T_p^{95} and T_p^{99} are ~5 s shorter than independent T_p^{95} and T_p^{99} (Fig. 13a, and d), and are projected to decrease under RCP 8.5, in contrast to projections of independently-derived T_p^{95} and T_p^{99}. The latter observation is expected since a best-fit conditional relationship between H_s and T_p was imposed. The findings are consistent with previous studies that have assessed changes in conditionally-derived extreme T_p (e.g., Cheng et al., 2015).

5. Summary and discussion

The findings of this study indicate that, over the course of the 21st century, mean annual wave heights will decrease along most of the North American west coast and south of Hawaii and increase north of Hawaii and within the Gulf of Alaska, under both RCP 4.5 and RCP 8.5. Mean wave periods are projected to increase along most of the ENP coast, except north of Hawaii. Extreme wave conditions exhibit a similar pattern along the mainland coast, where H_s^{95} are projected to decrease south of ~50°N and increase to the north under RCP 8.5. Results for the stabilizing radiative forcing scenario, RCP 4.5, are similar but less pronounced and yield little to no change between 45°N and 50°N and south of Hawaii.

The results presented here are consistent with some earlier studies, but differ compared to others, as there is a large variance in projected change patterns amongst other climate downscaling studies.

Table 5
Similarities of annual ΔH_s in coastal regions of the ENP between this and previous studies. (d:decreasing; i: increasing; 0: no change) (letters in italics indicate that the trend is the same as the multi-model mean projected in this study).

Type of downscaling	Abbreviation	West coast N. America	Gulf of AK	North of HI	South of HI	Paper figure
Dynamical	**This study**	**d**	**i**	**i**	**d**	7
	MEA10	*d*	0	d	*d*	SM-8
	HEA12-1	0	d	0	*d*	SM-8
	HEA12-2	*d*	d	d	*d*	SM-8
	FEA12-1	0	0	0	*d*	SM-8
	FEA12-2	*d*	0	0	*d*	SM-8
	SEA12	0	0	d	*d*	SM-8
	DOB12[a]	*d*	*i*	d	*d*	2e,f
	HEM13[b]	*d*	d	d	*d*	2b
	SEA13	*d*	*i*	d	*d*	7b
Statistical	WAS06-1	i	d	*i*	*d*	SM-8
	WAS06-2	i	0	*i*	*d*	SM-8
	WAS06-3	i	d	*i*	*d*	SM-8
	WAS06-4	i	0	*i*	*d*	SM-8
	WAS06-5	i	0	*i*	*d*	SM-8
	WAS06-6	i	d	*i*	*d*	SM-8
	WAS06-7	i	0	*i*	*d*	SM-8
	WAS06-8	i	d	*i*	*d*	SM-8
	WAS06-9	i	d	*i*	*d*	SM-8
	WAS06-10	0	0	0	*d*	SM-8
	WAS06-11	0	*i*	d	0	SM-8
	WAS06-12	i	0	*i*	*d*	SM-8
	WAS06-13	i	0	0	*d*	SM-8
	WAS06-14	i	0	*i*	i	SM-8
	MEA13	i	*i*	*i*	*d*	8
	WEA14	*d*	d	*i*	*d*	2a

SM-8: refers to a supplementary material figure in Hemer et al. (2013a).
MEA10: Mori et al. (2010); HEA12: Hemer et al., (2013b); FEA12: Fan et al. (2012); SEA12: Semedo et al. (2013); DOB12: Dobrynin et al. (2012); HEM13: Hemer et al. (2013a); SEA13: Semedo et al. (2013); WAS06: Wang and Swail (2006); MEA13: Mori et al. (2013); WEA14: Wang et al. (2014).
[a] A pre-industrial reference period was used in this study; all other studies employed a 20th century reference period.
[b] Ensemble mean of dynamical and statistical downscaling models.

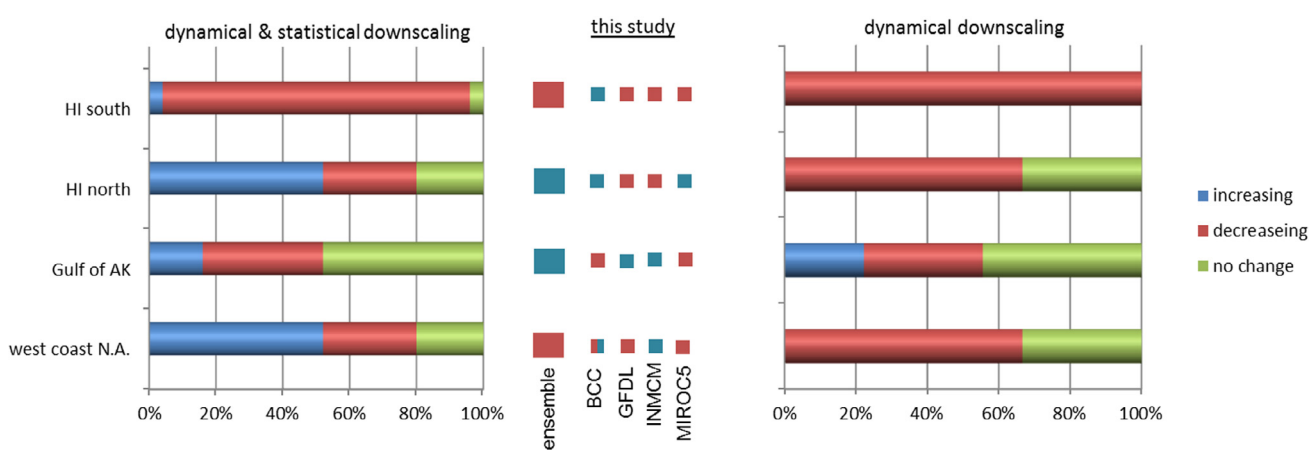

Fig. 14. Percent of studies that project increasing, decreasing, or no change in $\overline{H_s}$ by coastal regions of the ENP: (a) including all statistical and dynamical downscaling models; (b) dynamical downscaling models only. Projected trends attained as part of this study are shown in the middle: $\overline{H_s}$ are projected to decrease along the west coast of North America (Canada and U.S.A. conterminous west coasts) and south of Hawaii; $\overline{H_s}$ are projected to increase north of Hawaii and within the Gulf of Alaska. Studies included in the figure are listed in Table 5.

Because forcing scenarios and methods of implementation (e.g., statistical versus dynamical), analysis, and presentation of results differ between studies, it is difficult to make direct comparisons and thus only gross patterns of spatial $\Delta\overline{H_s}$ are compared. Table 5 and Fig. 14 summarize the general behavior (increasing, decreasing, or no change) of projected trends for four coastal regions where starkly different patterns were obtained: Gulf of Alaska, conterminous west coasts of Canada and the U.S., and north and south of Hawaii. The study by Dobrynin et al. (2012) differs from other studies in that a pre-industrial time-period (1850–1870) was used as a reference to derive change. Results from that study projected patterns of change similar to our projections under both RCP 4.5 and RCP 8.5. Interestingly, Dobrynin et al. (2012) found increased $\overline{H_s}$ for a hindcast period of 1989–1999 and consistent with historical buoy measurements within the ENP (see Section 1).

Projected decreases in ENP $\overline{H_s}$ are prevalent throughout the dynamical downscaling studies. With the exception of the Gulf of Alaska, all of the dynamical downscaling studies project no change or decreasing ENP $\overline{H_s}$ (Table 5; Fig. 14). Starting with the first dynamical global wave climate projection, Mori et al. (2010) projected decreases in $\overline{H_s}$ throughout the ENP, except in the area immediately surrounding the Aleutian Islands. Results from Mori et al. (2010) were used by Hemer et al. (2013a) in a seminal paper that presented ensemble results from three additional dynamical downscaling

studies (Fan et al., 2013; Hemer et al., 2013b; Semedo et al., 2013) plus 14 statistically downscaled projections (Wang and Swail, 2006). The ensemble results exhibited spatially consistent decreases throughout the ENP, but similar to the work presented here, there was a great deal of variance amongst the models (Hemer et al., 2013a).

Graham et al. (2013) conducted a dynamical downscaling study with a particular focus on the Canadian and U.S. west coasts using winds simulated by three GCMs under the 2007 IPCC A2 scenario to force WW3 on the global NWW3 grid. Their results, based on projected H_s^{95} and H_s^{99} during January through March, exhibit strong latitudinal dependencies with 10–15% decreases in H_s^{99} south of 40–45°N (Graham et al., 2013). At higher latitudes, Graham et al. (2013) projected increases in H_s^{95} and H_s^{99}, although patterns were less uniform. The findings of Graham et al. (2013) closely reflect our findings, particularly with respect to changes in H_s^{99} with latitude, high agreement between models projecting decreasing H_s^{99} to the south, and lower confidence but general increases to the north. In this study, the transition zone was found to be 5–10° further north and H_s^{99} decreases are projected to be smaller, on the order of < 5%.

Considering results from earlier works and the addition of results from this study, there are a growing number of studies that tend toward the projection that $\overline{H_s}$ will undergo little change or decrease along the west coasts of Canada and the U.S. during the 21st Century. Results from this study are also consistent with nearly all other previous studies, which indicate decreasing $\overline{H_s}$ south of Hawaii. North of Hawaii and within the Gulf of Alaska, model results show more disagreement and future conditions are more uncertain.

6. Conclusions

Near-surface winds simulated by four separate CMIP5 GCMs (BCC-CSM1.1, INM-CM4, MIROC5, and GFDL-ESM2M) under two climate change scenarios, RCP 4.5 and RCP 8.5, were used as inputs to the WaveWatch III numerical wave model. Wave simulations were completed on the NWW3 global grid (1° × 1.25°) and a one-way coupled ENP grid (0.25° × 0.25°). Though the entire globe was included in simulations, the focus of this study was the ENP coastline (south coast of Alaska, west coast of Canada and the U.S., and Hawaii). RCP 4.5 and RCP 8.5 characterize global radiative forcing by 2100 relative to the pre-industrial (1850) period and represent intermediate and high radiative forcing pathways, respectively. The wind-wave climate was modeled for three time-periods: historical (1976–2005), mid-century (2026–2045), and end-of-century (2081–2100). All results presented use the combined mid- and end-of-century time-periods for a single representation of the future. The overall aim of this study was to evaluate possible changes in the wave climate along the coasts within the ENP in response to climate change. The primary findings are as follows:

- The projected multi-model means of near-surface wind speeds are similar under both RCP 4.5 and RCP 8.5 within the Pacific Ocean basin: increases in wind speed in the northern and southern storm regions and small regions of decreases or no change in the remaining parts of the Pacific.
- Mean annual wave heights are projected to increase along the southern Alaska coast and northeast of Hawaii by >0.5 m and to decrease elsewhere. Increases in mean annual wave periods of 1–2 s for the mainland coast and >2 s south of Hawaii are projected. Inter-model agreement is high over approximately half the coastline.
- Extreme wave heights, represented by upper quantiles and extreme return period estimates, are projected to decrease along ENP coasts south of ~50°N. Projections under RCP 8.5 consistently yield greater changes compared to projections under RCP 4.5, the stabilization scenario, and indicate that the wave climate is responding to the climate change signal. North of ~50°N and within the Gulf of Alaska, results suggest weak, but increasing extreme wave heights. Upper quantile peak periods are projected to increase along the entire study area. Inter-model confidence is high south of ~45°N under both RCP 4.5 and RCP 8.5, though projected changes are small (<0.5 s).
- Incident wave directions associated with extreme wave heights are projected to rotate clockwise at the eastern end of the Aleutian Islands and counterclockwise offshore of Southern California. It is speculated that the clockwise rotation near the Aleutian Islands is in response to a northward and/or westward displacement of storm tracks and that the counterclockwise rotation offshore of Southern California is a reflection of decreasing wave energy from North Pacific-generated storms and the concurrent increase of Southern Ocean energy.

Projected changes to ENP wave conditions are conceptually similar to several previous works that have evaluated the response of waves to climate change: decreasing annual mean wave heights along most of the coast except Alaska (Dobrynin et al., 2012; Graham et al., 2013; Hemer et al., 2013a; Mori et al., 2013, 2010); increasing annual mean peak or mean periods (Hemer et al., 2013a); increasing extreme wave heights in the Gulf of Alaska and decreasing extreme wave heights elsewhere (Dobrynin et al., 2012; Fan et al., 2013; Graham et al., 2013). Yet, other studies have noted different patterns, either in projected mean or extreme wave heights, peak periods, or mean periods (Caires et al., 2006; Semedo et al., 2013; Wang et al., 2014; Wang and Swail, 2006). Some studies show similarities with one parameter, but not another. To address these differences and to try to reduce uncertainty, a larger suite of wave climate projections using atmospheric forcing from different climate models, from multiple runs from each of these models, and from different radiative pathways is needed. In an effort to support a framework that enables systematic validation, inter-comparison, and improved estimates and uncertainty of wave projections, the Coordinated Ocean Wave Climate Project (COWCLIP; Hemer et al., 2012) was established. The global and regional dynamical wave downscaling results of this study contribute to the COWCLIP ensemble effort (Hemer et al., in this issue).

Acknowledgments

We thank Jorge Perez of IH Cantabria for assistance in model evaluation. We also thank Sean Vitousek and Joseph Long of USGS and two anonymous reviewers who provided helpful constructive suggestions and criticisms. We acknowledge the World Climate Research Programme's Working Group on Coupled Modeling, which is responsible for CMIP, and we thank the climate modeling groups (listed in Table 1 of this paper) for producing and making available their model output. This work was funded by the USGS Coastal and Marine Geology Program.

References

Adams, P.N., Inman, D.L., Graham, N.E., 2008. Southern California deep-water wave climate: characterization and application to coastal processes. J. Coast. Res. 24, 1022–1035.
Ahrens, J.P., 1981: Irregular Wave Runup on Smooth Slopes. CETA No. 81-17. US Army Corps of Engineers, Coastal Engineering Research Center, Fort Belvoir, VA.
Allan, J.C., Komar, P.D., 2000. Are ocean wave heights increasing in the Eastern North Pacific? EOS, Trans. Am. Geophys. Union 81, 561–567.
Allan, J.C., Komar, P.D., 2006. Climate controls on US West Coast erosion processes. J. Coast. Res. 22, 211–529.
Alves, J.-H.G.M., 2006. Numerical modeling of ocean swell contributions to the global wind-wave climate. Ocean Modell. 11, 98–122.
Barnard, P.L., van Ormondt, M., Erikson, L.H., Eshleman, J., Hapke, C., Ruggiero, P., Adams, P.N. and Foxgrover, A.C., 2014. Development of the Coastal Storm Modeling System (CoSMoS) for predicting the impact of storms on high-energy, active-margin coasts. *Natural Hazards* in press.
Barnes, E.A., Polvani, L., 2013. Response of the midlatitude jets, and of their variability, to increased greenhouse gases in the CMIP5 models. J Climate 26, 7117–7135.

Bromirski, P.D., Cayan, D.R., Flick, R.E., 2005. Wave spectral energy variability in the northeast Pacific. J. Geophys. Res. 110.
Bromirski, P.D., Cayan, D.R., Helly, J., Wittmann, P., 2013. Wave power variability and trends across the North Pacific. J. Geophys. Res.:Oceans 118, 6329–6348.
Caires, S., Swail, V.R., Wang, X.L., 2006. Projection and analysis of extreme wave climate. J. Clim. 19, 5581–5605.
Caires, S., Sterl, A., 2004. 100-Year return value estimates for ocean wind speed and significant wave height from the ERA-40. J. Clim. 18, 1032–1048.
Callaghan, D.P., Nielsen, P., Short, A., Ranasinghe, R., 2008. Statistical simulation of wave climate and extreme beach erosion. Coast. Eng. 55, 375–390.
Cavaleri, L., Fox-Kemper, B., Hemer, M., 2012. Wind-waves in the coupled climate system. Bull. Am. Meteorol. Soc. 93, 1651–1661.
Cayan, D., M. Tyree, M.D. Dettinger, H. Hidalgo, T. Das, E.P. Maurer, P.D. Bromirski, N.E. Graham, and R.E. Flick, 2009: Climate change scenarios and sea level rise estimates for the California 2009 climate change scenarios assessment.
Cayan, D.R., Maurer, E.P., Dettinger, M.D., Tyree, M., Hayhoe, K., 2008. Climate change scenarios for the California region. Clim. Change 87, 21–42.
Chang, E.K.M., Guo, Y., Xia, X., Zheng, M., 2013. Storm-track activity in IPCC AR4/CMIP3 model simulations. J. Clim. 26, 246–260.
Chawla, A., Spindler, D.M., Tolman, H.L., 2013. Validation of a thirty year wave hindcast using the Climate Forecast System Reanalysis winds. Ocean Modell. 70, 189–206.
Cheng, T.K., Hill, D.F., Beamer, J., García-Medina, G., 2015. Climate change impacts on wave and surge processes in a Pacific Northwest (USA) estuary. J. Geophys. Res.:Oceans 120, 182–200.
Dee, D.P., Coauthors, 2011. The ERA-Interim reanalysis: configuration and performance of the data assimilation system. Q. J. R. Meteorol. Soc. 137, 553–597.
Dobrynin, M., Murawsky, J., Yang, S., 2012. Evolution of the global wind wave climate in CMIP5 experiments. Geophys. Res. Lett. 39.
Elguindi, N., Grundstein, A., 2013. An integrated approach to assessing 21st century climate change over the contiguous U.S. using the NARCCAP RCM output. Clim. Change 117, 809–827.
Fan, Y., Held, I.M., Lin, S.-J., Wang, X.L., 2013. Ocean warming effect on surface gravity wave climate change for the end of the twenty-first century. J. Clim. 26, 6046–6066.
Fan, Y., Lin, S.-J., Held, I.M., Yu, Z., Tolman, H.L., 2012. Global ocean surface wave simulation using a coupled atmosphere–wave model. J. Clim. 25, 6233–6252.
Favre, A., Gershunov, A., 2009. North Pacific cyclonic and anticyclonic transients in a global warming context: possible consequences for Western North American daily precipitation and temperature extremes. Clim. Dyn. 32, 969–987.
Feng, S., Hu, Q., Huang, W., Ho, C.-H., Li, R., Tang, Z., 2014. Projected climate regime shift under future global warming from multi-model, multi-scenario CMIP5 simulations. Glob. Planet. Change 112, 41–52.
Gemmrich, J., Thomas, B., Bouchard, R., 2011. Observational changes and trends in northeast Pacific wave records. Geophys. Res. Lett. 38, L22601.
Graham, N.E., Diaz, H.F., 2001. Evidence for intensification of North Pacfic winter cyclones since 1948. Bull. Am. Meteorol. Soc. 82, 1869–1893.
Graham, N.E., Cayan, D.R., Bromirski, P.D., Flick, R.E., 2013. Multi-model projections of twenty-first century North Pacific winter wave climate under the IPCC A2 scenario. Clim. Dyn. 40, 1335–1360.
Gulev, S.K., Grigorieva, V., 2006. Variability of the winter wind waves and swell in the North Atlantic and North Pacific as revealed by the voluntary observing ship data. J. Clim. 19, 5667–5685.
Hasselmann, S., Hasselmann, K., Allender, J.H., Barnett, T.P., 1985. Computations and parameterizations of the nonlinar energy transfer in gravity-wave spectrum, Part I: a new method fo refficient computations of the exact nonlinear transfer integral. J. Phys. Oceanogr. 15, 1369–1377.
Hemer, M.A., Katzfey, J., Trenham, C.E., 2013b. Global dynamical projections of surface ocean wave climate for a future high greenhouse gas emission scenario. Ocean Modell. 70, 221–245.
Hemer, M.A., Wang, X.L., Weisse, R., Swail, V.R., 2012. Advancing wind-waves climate science. Bull. Am. Meteorol. Soc. 93, 791–796.
Hemer, M.A., Fan, Y., Mori, N., Semedo, A., Wang, X.L., 2013a. Projected changes in wave climate from a multi-model ensemble. Nat. Clim. Change 3, 471–476.
Hibbard, K.A., Meehl, G.A., Cox, P.M., Friedlingstein, P., 2007. A strategy for climate change stabilization experiments. EOS: Trans. Am. Geophys. Union 88, 217–221.
Izaguirre, C., Méndez, F.J., Menéndez, M., Losada, I.J., 2011. Global extreme wave height variability based on satellite data. Geophys. Res. Lett. 38, L10607.
Jien, J.Y., Gough, W.A., Butler, K., 2015. The influence of El Niño–Southern Oscillation on tropical cyclone activity in the eastern north pacific basin. J. Clim. 28, 2459–2474.
Martucci, G., Carniel, S., Chiggiato, J., Sclavo, M., Lionello, P., Galati, M.B., 2010. Statistical trend analysis and extreme distribution of significant wave height from 1958 to 1999 – an application to the Italian Seas. Ocean Sci. 6, 525–538.
Mase, H., 1989. Random wave runup height on gentle slopes. J. Waterw. Port Coast. Ocean Eng. 115, 649–661.
Maurer, E.P., Hidalgo, H.G., Das, T., Dettinger, M.D., Cayan, D.R., 2010. The utility of daily large-scale climate data in the assessment of climate change impacts on daily streamflow in California. Hydrol. Earth Syst. Sci. 14, 1125–1138.
Meehl, G.A., and K.A. Hibbard, 2007. A strategy for climate change stabilization experiments with AOGCMs and ESMs. WCRP Informal Report No. 3/2007, ICPO Publication No. 112, IGBP Report No. 57, World Climate Research Programme: Geneva, 35 pp.
Meinshausen, M., Coauthors, 2011. The RCP greenhouse gas concentrations and their extensions from 1765 to 2300. Clim. Change 109, 213–241.
Méndez, F.J., Menéndez, M., Luceño, A., Losada, I.J., 2006. Estimation of the long-term variability of extreme significant wave height using a time-dependent Peak Over Threshold (POT) model. J. Geophys. Res.: Oceans 111, C07024.
Menéndez, M., Méndez, F.J., Losada, I.J., Graham, N.E., 2008. Variability of extreme wave heights in the northeast Pacific Ocean based on buoy measurements. Geophys. Res. Lett. 35, L22607.
Mesquita, M.S., Atkinson, D.E., Hodges, K.I., 2010. Characteristics and variability of storm tracks in the North Pacific, Bering Sea, and Alaska. J. Clim. 23, 294–311.
Mori, N., Shimura, T., Yasuda, T., Mase, H., 2013. Multi-model climate projections of ocean surface variables under different climate scenarios—future change of waves, sea level and wind. Ocean Eng. 71, 122–129.
Mori, N., Yasuda, T., Mase, H., Tom, T., Oku, Y., 2010. Projection of extreme wave climate change under global warming. Hydrol. Res. Lett. 4, 15–19.
Moss, R.H., Coauthors, 2010. The next generation of scenarios for climate change research and assessment. Nature 463, 747–756.
National Oceanic and Atmospheric Administration, 2010: Adapting to Climate Change: A Planning Guide for State Coastal Managers. National Oceanic and Atmospheric Administration.
Raible, C.C., Stocker, T.F., Yoshimori, M., Renold, M., Beyerle, U., Casty, C., Luterbacher, J., 2005. Northern hemispheric trends of pressure indices and atmospheric circulation patterns in observations, reconstructions, and coupled GCM simulations. J. Clim. 18, 3968–3982.
Ruggiero, P., Komar, P.D., Allan, J.C., 2010. Increasing wave heights and extreme value projections: the wave climate of the US Pacific Northwest. Coast. Eng. 57, 539–552.
Sasaki, W., 2014. Changes in the North Pacific wave climate since the mid-1990s. Geophys. Res. Lett. 41, 7854–7860.
Semedo, A., Sušelj, K., Rutgersson, A., Sterl, A., 2011. A global view on the wind sea and swell climate and variability from ERA-40. J. Clim. 24, 1461–1479.
Semedo, A., Weisse, R., Behrens, A., Sterl, A., Bengtsson, L., Günther, H., 2013. Projection of global wave climate change toward the end of the twenty-first century. J. Clim. 26, 8269–8288.
Shimura, T., Mori, N., Mase, H., 2013. Ocean waves and teleconnection patterns in the Northern Hemisphere. J. Clim. 26, 8654–8670.
Sillmann, J., Kharin, V.V., Zhang, X., Zwiers, F.W., Bronaugh, D., 2013. Climate extremes indices in the CMIP5 multimodel ensemble: Part 1. Model evaluation in the present climate. J. Geophys. Res.: Atmos. 118, 1716–1733.
Splinter, K.D., Davidson, M.A., Goshani, A., Tomlinson, R., 2012. Climate controls on longshore sediment transport. Cont. Shelf Res. 48, 146–156.
Stockdon, H.F., Holman, R.A., Howd, P.A., Sallenger, A.H., 2006. Empirical parameterization of setup, swash, and runup. Coast. Eng. 53, 573–588.
Stopa, J.E., Cheung, K.F., 2014. Intercomparison of wind and wave data from the ECMWF Reanalysis Interim and the NCEP Cliamte Forecast System Reanalysis. Ocean Modell. 75, 65–83.
Taylor, K.E., Stouffer, R.J., Meehl, G.A., 2012. An overview of CMIP5 and the experiment design. Bull. Am. Meteorol. Soc. 93, 485–498.
Thompson, D.W.J., Wallace, J.M., 1998. The Arctic oscillation signature in the wintertime geopotential height and temperature fields. Geophys. Res. Lett. 25 (9), 1297–1300.
Tolman, H.L., Balasubramaniyan, B., Burroughs, L.D., Chalikov, D.V., Chao, Y.Y., Chen, H.S., Gerald, V.M., 2002. Development and implementation of wind generated ocean surface wave models at NCEP. Weather Forecast. 17 (2), 311–333.
Tolman, H.L., Chalikov, D.V., 1996. Source terms in a third-generation wind wave model. J. Phys. Oceanogr. 26, 2497–2518.
Trenberth, K., Hurrell, J., 1994. Decadal atmosphere–ocean variations in the Pacific. Clim. Dyn. 9, 303–319.
Ulbrich, U., Leckebusch, G.C., Pinto, J.G., 2009. Extra-tropical cyclones in the present and future climate: a review. Theor. Appl. Climatol. 96, 117–131.
Van Der Meer, J.W., Stam, C.-J.M., 1992. Wave runup on smooth and rock slopes of coastal structures. J. Waterw. Port Coast. Ocean Eng. 118, 534–550.
van Vuuren, D., Edmonds, J., Kainuma, M., Riahi, K., Weyant, J., 2011. A special issue on the RCPs. Clim. Change 109, 1–4.
Wang, X.L., Feng, Y., Swail, V.R., 2014. Changes in global ocean wave heights as projected using multimodel CMIP5 simulations. Geophys. Res. Lett. 41, 1026–1034.
Wang, X.L., Swail, V.R., 2001. Changes of Extreme wave heights in northern hemisphere oceans and related atmospheric circulation regimes. J. Clim. 14, 2204–2221.
Wang, X.L.L., Swail, V.R., 2006. Climate change signal and uncertainty in projections of ocean wave heights. Clim. Dynam. 26, 109–126.
Yin, J.H., 2005. A consistent poleward shift of the storm tracks in simulations of 21st century climate. Geophys. Res. Lett. 32, L18701.
Young, I.R., Zieger, S., Babanin, A.V., 2011. Global trends in wind speed and wave height. Science 332, 451–455.

Please cite this article as: L.H. Erikson et al., Projected wave conditions in the Eastern North Pacific under the influence of two CMIP5 climate scenarios, Ocean Modelling (2015), http://dx.doi.org/10.1016/j.ocemod.2015.07.004